

Normalizing Flows on the Product Space of $SO(3)$ Manifolds for Probabilistic Human Pose Modeling

Olaf Dünkel^{1,2}, Tim Salzmann³, Florian Pfaff⁴

¹ Max Planck Institute for Informatics, ² Karlsruhe Institute of Technology,

³ Technical University of Munich, ⁴ University of Stuttgart

oduenkel@mpi-inf.mpg.de, tim.salzmann@tum.de, pfaff@ias.uni-stuttgart.de

Abstract

Normalizing flows have proven their efficacy for density estimation in Euclidean space, but their application to rotational representations, crucial in various domains such as robotics or human pose modeling, remains under-explored. Probabilistic models of the human pose can benefit from approaches that rigorously consider the rotational nature of human joints. For this purpose, we introduce *HuProSO3*, a normalizing flow model that operates on a high-dimensional product space of $SO(3)$ manifolds, modeling the joint distribution for human joints with three degrees of freedom. *HuProSO3*'s advantage over state-of-the-art approaches is demonstrated through its superior modeling accuracy in three different applications and its capability to evaluate the exact likelihood. This work not only addresses the technical challenge of learning densities on $SO(3)$ manifolds, but it also has broader implications for domains where the probabilistic regression of correlated 3D rotations is of importance. Code will be available at <https://github.com/odunkel/HuProSO>.

1. Introduction

Modeling uncertainties in high-dimensional Euclidean product spaces is a well-explored research problem [5–7, 12, 13, 24]. However, these methods often fall short in representing problems with an inherent rotational nature. This limitation is evident in scenarios like correlated object rotations in a scene or the orientation of animals in swarm behaviors, where the problems are modeled by a product space of $SO(3)$ manifolds. A particularly relevant example is human pose modeling, a problem of multiple correlated joint rotations. Accurately modeling human poses as densities on the Cartesian product of such joint rotations holds significant value for various fields, including computer vision and robotics.

A probabilistic model defined on $SO(3)$ manifolds rep-

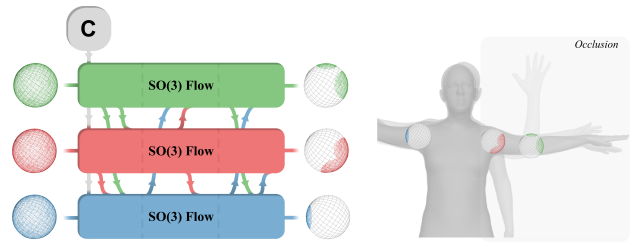


Figure 1. Application of the normalizing flow for occluded joints. Left: A normalizing flow defined on $SO(3)$ manifolds enables the learning of expressive human pose distributions, incorporating a context vector \mathbf{c} for conditioning. Right: Renderings of probable poses given condition \mathbf{c} , which is the observation of the human with the left arm occluded. The right arm’s pose is estimated with high certainty, while the left arm demonstrates varied but realistic poses due to the occlusion.

resenting joint rotation distributions is relevant for human pose and motion estimation. This model acts as a reliable prior in scenarios with unclear, noisy, incomplete, or absent observations [3, 14, 15, 29, 32], with an example being depicted in Fig. 1. Additionally, such a model is crucial in human-robot interaction for implementing risk-aware planning and control, necessitating the representation of human movements as normalized probabilistic densities [21].

Normalizing flows are recognized for their capability to learn normalized densities. Yet, their application has predominantly been in learning joint densities within Euclidean spaces, not fully addressing the properties of human pose, which is significantly influenced by the rotational nature of the human joints. Although some previous approaches in probabilistic human pose modeling have employed normalizing flows to learn distributions parameterized by rotational measures [14, 36], they fall short in learning normalized densities on the $SO(3)$. This is due to their Euclidean space-based approaches, which lack a continuous bijective mapping to $SO(3)$.

To overcome these shortcomings, we introduce a normalizing flow defined on the product space of $SO(3)$ man-

ifolds, accurately capturing the density of human joint rotations. By defining flow layers that explicitly operate on $\text{SO}(3)$, the learned density is normalized on the considered space of rotations with three degrees of freedom. The joint PDF on multiple $\text{SO}(3)$ manifolds expresses the statistical dependencies between human joints accordingly. To achieve this, the $\text{SO}(3)$ manifolds are explicitly linked using a nonlinear autoregressive conditioning not restricted to the common Gaussian setting.

We demonstrate that respecting the manifold structure of $\text{SO}(3)$ in the normalizing flow design improves the performance for multiple applications that involve a probabilistic model of human pose, outperforming state-of-the-art approaches in most configurations.

In summary, our work makes three key contributions:

- We present a normalizing flow model for learning normalized densities on the high-dimensional product space of $\text{SO}(3)$ manifolds. This is enabled by conceptualizing a flow layer that specifically operates on $\text{SO}(3)$ and lifting the model to a product space via an expressive nonlinear autoregressive conditioning approach.
- Introducing HuProSO3, a probabilistic **H**uman pose model on the **P**roduct Space of **SO(3)** manifolds, we elucidate the application of our presented normalizing flow model in various applications where a probabilistic model of humans is relevant.
- We showcase HuProSO3’s effectiveness and adaptability through applications like probabilistic inverse kinematics and 2D to 3D pose uplifting, outperforming several state-of-the-art methods in tasks involving probabilistic human pose models.

2. Related work

2.1. Normalizing Flows on Rotational Manifolds

Normalizing flows model complex distributions through a series of sequential flow layers. They learn a normalized density, represented by the change of variables formula:

$$p(x) = \pi(T^{-1}(x)) |J_{T^{-1}(x)}|, \quad (1)$$

where $J_{T^{-1}(\cdot)}$ is the Jacobi-matrix of the inverse of the diffeomorphic transformation $T : \mathbb{R}^d \rightarrow \mathbb{R}^d$ and its inverse $T^{-1}(\cdot)$, where a diffeomorphic transformation is invertible and both, T and its inverse T^{-1} , are differentiable.

Several methods adapt normalizing flows, typically applied in Euclidean spaces, for rotational manifolds, including $\text{SO}(3)$. Rezende et al. [27] successfully apply the Möbius transformation, circular splines, and a non-compact projection for learning densities on such manifolds. Falorsi et al. [8] develop a normalizing flow in Euclidean space that is then mapped to $\text{SO}(3)$, but this approach involves non-unique mappings from the Lie algebra to the Lie group. Contrarily, Liu et al. [18] propose a novel Möbius coupling

layer and quaternion affine transformation, facilitating the learning of normalizing flows directly on $\text{SO}(3)$.

Flows for Product Spaces of Rotational Manifolds. Papamakarios et al. [23] present a strategy for an autoregressive model that allows learning densities on high-dimensional Euclidean spaces. Building on this, Stimper et al. [33] introduced a PyTorch package for defining normalizing flows on Cartesian products of 1-spheres using two-dimensional embeddings of angular quantities. However, this method does not extend to general n -spheres or $\text{SO}(3)$ manifolds. Additionally, Glösenkamp [11] facilitated learning on rotational manifolds, including tori and 2-spheres, using an autoregressive conditioning approach. Yet, his framework is limited by a fixed conditioning sequence and lacks support for flows on $\text{SO}(3)$ manifolds.

2.2. Learning Human Pose Distributions

In the domain of human pose estimation, models traditionally use joint rotations as parameters [1, 16] to reflect the skeleton’s rotational characteristics. Pioneering methods for learning the unconditional human pose distribution include a GMM [2] and a VAE [25], both proving effective as pose priors. Later advancements utilized normalizing flows in Euclidean space [36] using the 6D representation [38].

Subsequent works [4, 34] that learn a human pose prior have highlighted the inadequacy of a Gaussian assumption for the joint rotation parameterization due to their unbounded nature. So, they propose different ways to account for this issue in the design of their generative models for the human pose. Davydov et al. [4] show that a spherical noise distribution in the latent space of GAN-based approach results in a distribution with more realistic human poses and a smoother latent space. Tiwari et al. [34] model a manifold on the product space of $\text{SO}(3)$ that represents the set of feasible human poses.

Probabilistic techniques have been effectively employed to infer human pose distributions from image inputs [14, 30–32]. Sengupta et al. [30] utilize the Matrix-Fisher distribution for learning the rotational distributions of individual joints on $\text{SO}(3)$. Meanwhile, Kolotouros et al. [14] model joint rotations using a 6D representation and employ normalizing flows to learn densities, incorporating an additional loss term to account for the orthonormality of the columns in the 6D representation. Sengupta et al. [32] present a novel approach to model human pose distributions on the product space of $\text{SO}(3)$. This method factorizes the joint PDF by using autoregressive conditioning along the human kinematic tree. It respects the manifold structure of joint rotations by learning a normalizing flow on the Lie algebra and subsequently mapping it to the Lie group. Voleti et al. [35] builds upon [22] to model the pose and applies it, e.g., to inverse kinematics from sparse 3D key points.

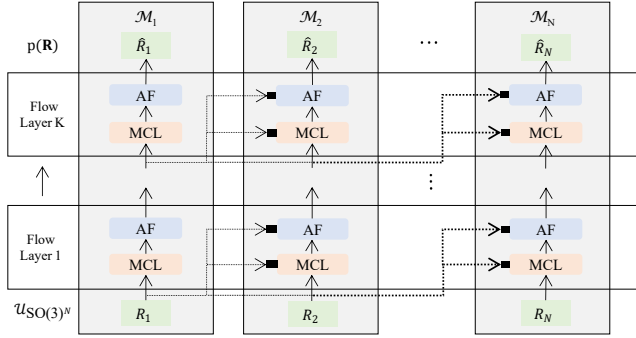


Figure 2. Overview of the components of the normalizing flow: The flow is defined on a product space of N manifolds $\mathcal{M}_i = SO(3)$. It includes K flow layers that transform samples R_i from a uniform distribution on $SO(3)$ to samples of the learned distribution \hat{R}_j . The flow is composed of a Möbius coupling layer (MCL) and a quaternion affine transformation (AF). Vertical arrows indicate the flow of $SO(3)$ samples through layers, while dotted arrows represent autoregressive conditioning using an MLP (black boxes).

3. Method

In this section, we describe our method for deriving and implementing the following desiderata: First, as outlined in Sec. 3.2, each normalizing flow layer is designed to respect and operate within the $SO(3)$ manifold. Second, we ensemble these individual flow layers to model a density on the product space of $SO(3)$ manifolds. Finally, we present the probabilistic human pose model HuProSO3, which comprises and instantiates the aforementioned methodology.

3.1. Problem Statement

Given the special orthogonal group $SO(3)$ that is defined as the set of rotation matrices \mathbf{R}

$$\{\mathbf{R} \in \mathbb{R}^{3 \times 3} \mid \mathbf{R}^T \mathbf{R} = \mathbf{I}, \quad \det \mathbf{R} = 1\}, \quad (2)$$

we aim to learn a PDF $p(\mathbf{R}|\mathbf{c})$, where the random variable $\mathbf{R} = [\mathbf{R}_1, \dots, \mathbf{R}_N]$ is defined on a product space $\mathbf{P} = \prod_i^N \mathcal{M}_i$ of N $SO(3)$ manifolds $\mathcal{M}_i = SO(3)$ and the context vector $\mathbf{c} \in \mathbb{R}^L$ conditions the PDF.

3.2. Normalizing Flows on a Product Space of $SO(3)$ Manifolds

The structure of our model, as illustrated in Fig. 2, involves multiple flow layers that convert a uniform density on $SO(3)$ into the target density for each manifold $\mathcal{M}_i = SO(3)$. Samples R_i are drawn from a uniform distribution on $SO(3)$. Then, the samples are mapped to the target distribution \hat{R}_i through the sequential application of diffeomorphic flow layers. The normalizing flow is trained by maximizing the likelihood of the target sample that is propagated through the flow layers (NLL Loss).

The manifolds are connected in an autoregressive manner to allow for learning a joint PDF. The flow is defined

on $SO(3)$ by leveraging a Möbius coupling layer and a quaternion affine transformation [18] as invertible flow layers on $SO(3)$. The joint likelihood of the product space \mathbf{P} is learned using randomly masked nonlinear autoregressive conditioning. We present these mechanisms in more detail in the following.

Möbius Coupling Layers. The core principle of normalizing flows involves applying diffeomorphic transformations in each layer, which ensures that the original density remains normalized. However, defining these transformations for the $SO(3)$ manifold, unlike in Euclidean space, presents challenges. We must ensure that both the forward transformation and its inverse operate on $SO(3)$ and do not map to points outside this manifold. To this end, we apply the Möbius transformation, which expresses parameterized distributions on spheres.

A rotation matrix $R \in SO(3)$ can be described using any two of its three orthonormal three-dimensional unit column vectors $(\mathbf{x}_1|\mathbf{x}_2|\mathbf{x}_3)$ [38]. Thus, each column represents a three-dimensional unit vector defined on the unit sphere $\mathbf{x}_i \in \mathcal{S}^2$, $i \in \{1, 2, 3\}$, parameterized in Euclidean coordinates $\mathbf{x}_i \in \mathbb{R}^3$.

The Möbius transformation of a point $\mathbf{y} \in \mathcal{S}^D$, given a parameter $\omega \in \mathbb{R}^{D+1}$, is defined as

$$h_\omega(\mathbf{y}) = h(\omega, \mathbf{y}) = \frac{1 - \|\omega\|^2}{\|\mathbf{y} - \omega\|}. \quad (3)$$

It projects a point \mathbf{y} to a new location on the same sphere \mathcal{S}^D . The Möbius transformation is leveraged to design the Möbius coupling layer [18]—an invertible flow layer on $SO(3)$ that transforms a valid rotation matrix $R = (\mathbf{x}_1|\mathbf{x}_2|\mathbf{x}_3)$ into a different valid rotation matrix $R' = (\mathbf{x}'_1|\mathbf{x}'_2|\mathbf{x}'_3)$. The Möbius coupling layer ensures orthogonality in the transformed rotation matrix as follows: The first column $\mathbf{x}'_1 = \mathbf{x}_1$ remains unchanged, providing the basis for adapting the second column vector. This second column, modeled as a point $\mathbf{x}_2 \in \mathcal{S}^2$ is transformed into a new point $\mathbf{x}'_2 = h(\omega_{\mathbf{x}_1}, \mathbf{x}_2) \in \mathcal{S}^2$, using the Möbius transformation. The transformation parameter

$$\omega_{\mathbf{x}_1} = \xi(\mathbf{x}_1) = g(\mathbf{x}_1) - \mathbf{x}_1 (\mathbf{x}_1 \cdot g(\mathbf{x}_1)) \quad (4)$$

is derived from \mathbf{x}_1 . Here, $g(\cdot) \in \mathbb{R}^3$ represents an MLP output, projected onto a plane perpendicular to \mathbf{x}'_1 . Consequently, the resulting column vector \mathbf{x}'_2 is orthogonal to \mathbf{x}'_1 . The final step in constructing the rotation matrix involves computing the third column, \mathbf{x}'_3 , using the cross product $\mathbf{x}'_3 = \mathbf{x}'_1 \times \mathbf{x}'_2$. This ensures the completion of the rotation matrix R' with a vector orthogonal to the first two columns.

In a rotation matrix, the first column specifies two out of three rotational degrees of freedom, while the second column determines the remaining degree. Since the first column \mathbf{x}_1 remains unchanged in a single Möbius coupling layer, each layer only modifies the rotation along one degree of freedom. To address this, we employ permutations

in the conditioning sequence of consecutive flow layers. For example, we use the Möbius transformation to derive a new column $\mathbf{x}'_1 = f(\omega_{\mathbf{x}_2}, \mathbf{x}_1)$, where $\omega_{\mathbf{x}_2}$ is calculated from \mathbf{x}_2 . By applying such permutations changes for several flow layers all rotational degrees of freedom can be modeled. These permutations, being invertible and volume-preserving transformations with an absolute Jacobian of 1 [24], can be integrated into normalizing flows.

While a single Möbius coupling layer effectively warps distributions on $SO(3)$ nonlinearly, it only transforms one rotational degree of freedom via the second column of a rotation matrix. However, this strategy does not directly allow the modification of multiple rotational degrees simultaneously by moving or scaling distributions on $SO(3)$, as [18] illustrates. To account for this, we also apply an affine quaternion transformation [18] in our normalizing flow.

Quaternion Affine Transformation. The quaternion affine transformation allows learning an affine transformation on the 3-sphere, a double-cover of $SO(3)$. It, thus, realizes a global rotation and a shifting operation on $SO(3)$. The quaternion affine transformation

$$f_q(\mathbf{q}) = W\mathbf{q} \cdot (\|W\mathbf{q}\|)^{-1} \quad (5)$$

is applied to a quaternion $\mathbf{q} = m_{\mathbf{R} \rightarrow \mathbf{q}}(\mathbf{R})$, where \mathbf{q} is computed from the considered rotation matrix \mathbf{R} and the invertible 4×4 matrix W is constructed using *svd* decomposition. The parameters of the matrices of the *svd* decomposition are learned during training. As shown in Fig. 2, this transformation follows each Möbius coupling layer. Maintaining the quaternion’s real part positive is required for the transformation’s invertibility. This constraint does not hinder expressiveness, as \mathbf{q} and $-\mathbf{q}$ denote the same rotation.

Joint PDF on a Product Space. While the described Möbius and affine quaternion transformations effectively operate on a single $SO(3)$ manifold, they do not suffice to construct a normalizing flow for the product space $\mathbf{P} = \prod_i^N SO(3)$. We address this by introducing an autoregressive masking strategy, designed to learn a joint PDF on such a product space. Masked autoregressive flows [24] learn PDFs defined on n -dimensional Euclidean spaces $\mathbf{z} \in \mathbb{R}^n$. They implement autoregressive conditioning by applying consecutive MADE [10] blocks for linking different dimensions with the Gaussian conditionals parameterized by

$$z_i = u_i \exp f_{\alpha_i}(\mathbf{z}_{1:i-1}) + f_{\mu_i}(\mathbf{z}_{1:i-1}), \quad (6)$$

with the scalar functions $f(\cdot)$ that output the mean and log standard deviation of the conditional i given all previous dimensions. The term $u_i \sim \mathcal{N}(0, 1)$ represents noise.

The expression in Eq. (6) links individual dimensions. However, this approach does not account for manifolds that cannot be expressed by Cartesian products in Euclidean space, e.g., the 2-sphere or $SO(3)$. Using standard Gaussian conditionals falls short in capturing the dependencies of non-Euclidean manifolds.

To address these challenges, we first apply autoregressive conditioning based on random variables defined on $SO(3)$. For this purpose, the joint density is decomposed autoregressively:

$$p(\mathbf{R}) = \prod_i^N p(\mathbf{R}_i | \mathbf{R}_{1:i-1}), \quad (7)$$

where each conditional is defined on $\mathbf{R}_i \in SO(3)$ and conditioned on preceding $SO(3)$ manifolds $\mathbf{R}_{1:i-1} \in \prod_1^{i-1} SO(3)$. Such a decomposition is generally restricted to a fixed order of conditioning, which does not capture arbitrary dependencies between different $SO(3)$ manifolds. To mitigate this problem, we randomly vary the order of conditioning in each flow layer, similar to [23], which results in more expressive flows [24]. We achieve this by permuting the $SO(3)$ rotation sequences between autoregressive layers, leveraging the invertibility of permutations.

Instead of using a linear coupling with the conditionals parameterized as Gaussians for Euclidean space as proposed in [23] and expressed in Eq. (6), we compute the parameters of the considered manifold \mathcal{M}_i autoregressively. This involves a nonlinear map $g_c(\mathbf{x}_{12}^{(1:i-1)})$ with parameters learned during training to condition the current manifold’s distribution on the preceding ones. We parameterize the $SO(3)$ rotations of previous dimensions $\mathbf{R}_{1:i-1}$ in the continuous 6D representation [38] with $\mathbf{x}_{12}^{(i:i-1)}$. This conditioning is then integrated into both the affine transformation and the Möbius coupling layer.

The affine transformation is conditioned on the previous dimensions by using a neural network to compute the matrix $\mathbf{W}_i = g_{c-W}^{(i)}(\mathbf{x}_{12}^{(1:i-1)})$. We realize the autoregressive conditioning in the Möbius coupling layer by computing the parameters of the Möbius transformation based on the first rotation matrix’ column of the considered dimension $\mathbf{x}_1^{(i)} \in \mathbb{R}^3$ and the previous dimensions $\mathbf{x}_{12}^{(1:i-1)} \in \mathbb{R}^{3 \times 2 \times (i-1)}$ in 6D representation $g_{c-M}(\left[\mathbf{x}_1^{(i)}, \mathbf{x}_{12}^{(1:i-1)}\right])$.

Conditioning the Joint PDF. The joint PDF can be conditioned on additional information \mathbf{c} by augmenting the set of conditions of each term in the chain rule of probability with the condition \mathbf{c} :

$$p(\mathbf{R}|\mathbf{c}) = \prod_i p(\mathbf{R}_i | \mathbf{R}_{1:i-1}, \mathbf{c}). \quad (8)$$

3.3. Learning Human Pose Distributions

We leverage our normalizing flow to learn a probabilistic model of the human pose. We use the SMPL [2] model to parameterize the human pose with 21 joints. After removing static joints in the AMASS database, our model describes a density $p(\mathbf{R}|\mathbf{c})$ on a product space of $N = 19$ $SO(3)$ manifolds. We call this normalizing flow HuProSO3,

a probabilistic **H**uman pose model on the **P**roduct Space of **SO(3)** manifolds.

We deploy HuProSO3 in several applications, the first being to learn an unconditional human pose prior. In this case, we do not condition, i.e., $\mathbf{c} = \emptyset$. This pose prior acts as a generative model for sampling realistic human poses and can also be used for evaluating the probability of a specific pose that is parameterized by joint rotations $p(\mathbf{R} = \{R_{\text{joint},1}, \dots, R_{\text{joint},19}\})$. Second, we inject a condition \mathbf{c}_{feat} into the model to learn a density that is specific to a given context. To handle varying contexts and to remove computations in each flow layer, we add an additional MLP $\mathbf{c} = g(\mathbf{c}_{\text{feat}})$ that computes the relevant features that are injected into the normalizing flow, as outlined in Eq. (8). HuProSO3 generally supports arbitrary conditions. We present conditioning with 2D and 3D key points, where $\mathbf{c}_{\text{feat}} \in \mathbb{R}^{J \times k}$ with $J = 21$ joints and $k \in \{2, 3\}$ for conditioning with 2D and 3D key points.

To demonstrate HuProSO3’s ability to capture human pose distributions, we adapt the masking strategy from [3]. Parts of the context features $\mathbf{c}'_{\text{feat}} = \mathbf{m} \cdot \mathbf{c}_{\text{feat}}$ are removed by applying the mask $\mathbf{m} = [m_1, m_2, \dots, m_J]$ with $m_i \in \{0, 1\}$ indicating whether a joint position is accessible. To allow conditioning with an arbitrary number of joints during evaluation, we seek a different masking strategy to [3] and we mask each joint with varying probabilities $p_m \in [0, 1]$ during training. Therefore, the model has learned to handle varying numbers of occluded joints.

4. Experiments

While HuProSO3’s design ensures that all flow transformations are on $\text{SO}(3)$ and capture nonlinear dependencies between the $\text{SO}(3)$ manifolds, we now also demonstrate experimentally that it has sufficient expressiveness to accurately model human pose distributions. We, therefore, evaluate HuProSO3 on different applications that involve a probabilistic model of the human pose. First, we learn an unconditional human pose prior that showcases HuProSO3’s capability of learning the intricate distribution human poses.

Second, we condition the distribution demonstrating HuProSO3’s capabilities of injecting observations or other conditions for learning task-specific distributions and correctly adapting the respective uncertainties arising from different sources of conditioning. For this task, we also evaluate cases when only partial information is given. This includes scenarios with partial information, such as occluded joints, where HuProSO3 effectively reasons about uncertainties due to missing information.

4.1. Unconditional Pose Prior

To demonstrate HuProSO3’s effectiveness in an unconditional setting, we train a human pose prior using the

Table 1. Summary of precision and recall statistics for AMASS. The reported values represent the cumulative geodesic distances for all joint rotations between samples from the dataset and the evaluated pose prior.

	Test (mean [median])		Train (mean [median])	
	Recall	Precision	Recall	Precision
GAN-S [4]	3.76 [3.34]	4.51 [4.23]	3.57 [3.34]	4.38 [4.13]
6D NF	3.66 [3.16]	4.50 [4.00]	3.55 [3.32]	4.42 [4.10]
Ours	3.44 [2.95]	4.24 [3.71]	2.93 [2.64]	3.90 [3.59]

AMASS database [19] with its standard dataset split. We then compare its ability to generate realistic human poses against various other human pose priors.

Metrics. In general, the likelihood is the best metric for evaluating how well a model has learned a distribution. However, we are the first to provide normalized joint densities of the human pose distribution on $\text{SO}(3)$ manifolds. Therefore, our evaluation relies on comparing generated samples from HuProSO3 with those from previous approaches. We follow an experimental pipeline similar to [4] to evaluate whether human poses sampled from the considered pose prior deviate from samples from the dataset distribution (precision) and whether the pose prior has captured the variety of poses in the dataset (recall). For recall, we compare 1k dataset samples against 100k poses sampled from our model, calculating the minimum error (nearest neighbor). Precision is evaluated by comparing 100k dataset samples against 1k model-generated samples, again computing the minimum error for these model samples.

Since we aim to evaluate how well the model captures the distribution $p(\mathbf{R})$ on the product space of $\text{SO}(3)$, we evaluate precision and recall based on the sum of all $J = 21$ geodesic distances $d_{\text{geo}}(R_{i,k}, R_{j,k})$ of the rotations $R_{i,k}$ and $R_{j,k}$ that correspond to the k -th SMPL joint of pose i and j , respectively, where the geodesic distance is computed by

$$d_{\text{geo}}(R_{i,k}, R_{j,k}) = \arccos \frac{\text{tr}(R_{i,k}^T R_{j,k}) - 1}{2}. \quad (9)$$

Baselines. In our evaluation, HuProSO3 is compared with the GAN-S human pose prior [4] and a 6D normalizing flow similar to models in [36, 37]. We train GAN-S from scratch using the standard parameter configuration provided by [4]. To compare against a 6D normalizing flow, we trained an autoregressive [23] neural spline flow [7] using the normflows library [33]. We provide additional results for Pose-NDF [34] as a pose prior in see Tab. 8 (Appendix D.1).

Results. In Tab. 1, we present the mean and median of precision and recall for both, training and test datasets. The results illustrate that HuProSO3 has captured the training dataset’s distribution best. The means of precision and recall metric, both, are lower depicting that the model generates poses that correspond to realistic poses from the dataset

Table 2. MGEO [rad] and MPJPE [mm] results for the IK task on the AMASS test split. Performance comparisons are made for optimization-based (**best**) and probabilistic methods (**best**). Probabilistic methods are assessed using a single random sample and the average of 10 random samples.

Method	MPJPE (1 10)	MGEO (1 10)
VPoser [25]	26.6 -	0.230 -
GAN-S [4]	12.1 -	0.224 -
Pose-NDF [34]	0.2 -	0.289 -
HF-AC [32]	33.2 21.2	0.308 0.251
Ours	8.2 5.5	0.163 0.121

but it also captures the variety of the seen poses during training. We observe similar results for the median metric. Moreover, while having learned the training distribution more accurately, our model does not overfit and it outperforms other methods on the precision and recall metric for the test dataset as well. Precision and recall curves, log likelihood comparisons for training and test datasets, and qualitative joint correlation illustrations are provided in the appendix. Additionally, rendered poses in Fig. 12 confirm HuProSO3’s ability to generate realistic and diverse human poses (see Appendix C.3).

4.2. Inverse Kinematics

In this experiment, we condition the learned density on the 3D position of the $J = 21$ SMPL joints to solve the human pose inverse kinematic (IK) problem: The goal is to learn the PDF $p(\mathbf{R}|\mathbf{c})$ that is defined on $\text{SO}(3)$ and conditioned on the joint positions in 3D space $\mathbf{c} \in \mathbb{R}^{J \times 3}$.

Metrics. To assess the models, we use the Mean Geodesic Distance (MGEO) across joint rotations for rotational error and the Mean Per Joint Position Error (MPJPE) to evaluate the accuracy of learned densities in relation to error propagation in forward kinematics. Effective probabilistic models are expected to produce samples consistent with the given conditioning, with accuracy increasing upon evaluating more samples. Therefore, we test probabilistic methods using both a single random sample and an average of 10 random samples.

Baselines. We compare our approach against both, optimization-based and learning-based baselines by evaluating the MGEO and MPJPE metrics. We consider the following learned pose priors: We use the IK solver provided by [25] focusing solely on pose without shape optimization. Furthermore, we evaluate PoseNDF [34] utilizing the pre-trained model and the existing pipeline. As implemented in the published code by [34], we use the optimization objective

$$\mathcal{L}_{\text{IK}} = \sum_{k=1}^{N_{\text{test}}} \sum_{i=1}^J \|\mathbf{x}_{\text{gt},i,k} - \hat{\mathbf{x}}_{i,k}\|_2, \quad (10)$$

which compares the ground truth joint position i $\mathbf{x}_{\text{gt},i,k}$ with the predicted position $\hat{\mathbf{x}}_{i,k} = FK(\mathbf{R}_{i,k})$ after applying for-

Table 3. MPJPE | MGEO for different types of occlusions: Left leg (L), left arm and hand (A+H), and right shoulder and upper arm (S+UA).

Method	L	A+H	S+UA
Pose-NDF [34]	28.3 0.341	38.3 0.360	2.1 0.333
GAN-S [4]	16.8 0.240	29.6 0.260	18.8 0.241
HF-AC [32] (N=10)	101.3 0.289	81.4 0.301	72.2 0.270
Ours (N=10)	13.9 0.165	30.2 0.201	12.7 0.162

ward kinematics to the optimized rotation and all N_{test} samples of the test dataset. We utilize the optimization process from [34], omitting the temporal smoothness term.

Similarly, we use the trained GAN-S model and we optimize its latent code \mathbf{z} to minimize the loss in Eq. (10) with $\hat{\mathbf{x}}_i = \mathcal{G}(\mathbf{z})$ using the LBFGS optimizer [17].

In addition, we use the implementation of HuManiFlow [32], which implements the normalizing flow for learning the ancestor-conditioned density on a single $\text{SO}(3)$ manifold. Different from its original design, which conditions on visual features from a CNN encoder, we adapt it to condition on 3D keypoint positions and train the normalizing flow from scratch. We refer to it with HF-AC.

Results. The low errors, as depicted in Tab. 2, show that HuProSO3 is capable of respecting conditions accurately. Our probabilistic method has mostly comparable or better results than other pose priors optimized in latent space [4, 25]. Pose-NDF performs best on the MPJPE metric because it does not penalize a pose as long as it is realistic. For this reason, the optimization-based approach allows to match the given 3D key points nearly perfectly. However, the worse performance on the MGEO metric demonstrates that Pose-NDF models the manifold of plausible poses. Therefore, it cannot infer the most likely joint rotations for the given 3D key points, but it infers a rotation that belongs to the set of feasible joint rotations.

We evaluate the exact log-likelihood of HuProSo3 and HF-AC approach in Tab. 7 in Appendix D.1.

4.3. Inverse Kinematics with Partial Observation

We evaluate the capabilities of HuProSO3 to solve IK in the case of partially given 3D key points, e.g., when some joints are occluded. The rotational distribution of these joints can be inferred using a probabilistic human pose model. A joint PDF is essential for this task because it captures all statistical dependencies, which contrasts selecting a fixed sequence of conditioning, e.g., along the kinematic tree. We provide a dataset analysis in Appendix A. Following the methodology of [26, 34], we evaluate three examples of occlusions: the left leg (L), the left arm including the hand (A + H), and the right shoulder with the upper arm (S + UA).

We utilize the same HuProSO3 model across all experiments, conditioned on 3D keypoint positions and trained

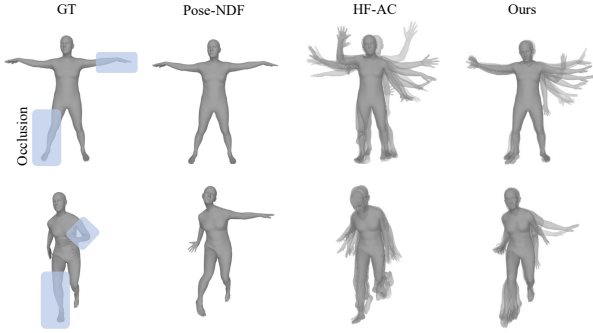


Figure 3. Qualitative results for inverse kinematics with partial occlusion (left arm and right leg). For the normalizing flow based models (HF AC and HuProSO3), we visualize 10 samples, where less likely poses are more transparent.

with the randomized masking strategy outlined in Sec. 3.3 to account for occluded joints. This approach enables the model to handle various occlusion scenarios effectively.

Metrics and Baselines. Similar to the IK setting elaborated above, we report MGEO and MPJPE and we compare with Pose-NDF and GAN-S, as detailed in Sec. 4.2. Additionally, we compare HuProSO3 to previously reported results based on the per-vertex error as in [26] and [34] (see Tab. 11 in Appendix D.4).

To account for the occluded joints, we mask the occluded joints in the optimization objective similar to the conditioning for HuProSO3 in Sec. 3.3 and we augment the optimization objective Eq. (10)

$$\mathcal{L}_{\text{IK}} = \sum_k^{N_{\text{test}}} \sum_i^J m_i \|\mathbf{x}_{\text{gt},i,k} - \hat{\mathbf{x}}_{i,k}\|_2, \quad (11)$$

with the mask $\mathbf{m} = [m_1, \dots, m_J]$, $m_i \in \{0, 1\}$, that cancels the contributions of the occluded joints to the loss term. The joint rotations are initialized randomly but close to 0, as stated in [34].

Results. We present the MGEO and MPJPE evaluation results in Tab. 3. Optimization-based methods Pose-NDF [34] and VPoser [25] are initialized with rotations close to the rest pose. For this reason, they perform significantly better for occluded legs, where the ground truth involves mostly straight legs. However, these methods yield higher errors when optimizing the more variable arm joints. In contrast, HuProSO3 demonstrates more accurate estimates across various types of occlusions. The results show HuProSO3 is excelling for all occlusion types on the MGEO metric. It better captures the distribution on the joint rotation space. We present the per-vertex errors in Tab. 11 in Appendix D.4.

Pose-NDF performs exceptionally well in cases of right shoulder and upper arm occlusions, likely due to the accurate optimization of arm joint rotations based on the given

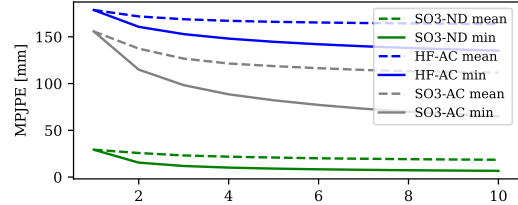


Figure 4. Minimum MPJPE and MPJPE of the mean pose for HuProSO3, ancestor-conditioned SO(3), and HF-AC for randomly occluded joints ($p_m = 0.3$) with varying numbers of samples.

Table 4. Evaluation results for the 5-point evaluation task in MPJPE [mm] and MGEO [rad]. We consider 1 sample and the average over 10 samples for HuProSO3.

Method	Pose-NDF [34]	GAN-S [4]	Ours (1 10)
MPJPE	37.8	46.5	36.4 27.3
MGEO	0.405	0.284	0.290 0.208

hand position. However, the MGEO metric is comparably high. As elucidated for the IK task, Pose-NDF does not represent a probabilistic model of the human pose but models the manifold of feasible poses. For this reason, the most likely joint rotation is not inferred, but only one possible rotation is computed. Therefore, large errors arise in particular for the rotations of the leaf joints (see, e.g., the right hand in the second row of Fig. 3).

GAN-S shows a lower MPJPE for occlusions of the left arm and hand, with performance comparable to HuProSO3 for other occlusions. This indicates the effectiveness of the latent code optimization in GAN-S, especially on the MPJPE metric. However, our model captures the joint rotation distribution more accurately, as the better MGEO metric depicts. In addition, our model predicts without the need for optimization on the joint positions, without being specifically trained for that particular type of occlusion, and it predicts in a probabilistic manner. To demonstrate how a varying number of randomly occluded joints affects performance, we refer to Fig. 14 in Appendix D.5.

For the scenario of occluded joints, HuProSO3 outperforms HF-AC on rotation- and position-based metrics. We reason that this is, firstly, due to HuProSO3 modeling the complete joint density while HuManiFlow [32] learns only the ancestor-conditioned distribution of individual joints. If we train our model with a fixed ancestor-conditioning, we still reach a better accuracy than HF-AC for randomly occluded joints (Fig. 4). See more details in Appendix D.5. We assume that designing the normalizing flow directly on SO(3) contributes to the better performance.

Fig. 3 illustrates qualitative results for IK with occluded joints. HuProSO3 accounts for the ambiguous nature of the task: While visible joints only have a low diversity, occluded joint result in diverse but likely predictions. We

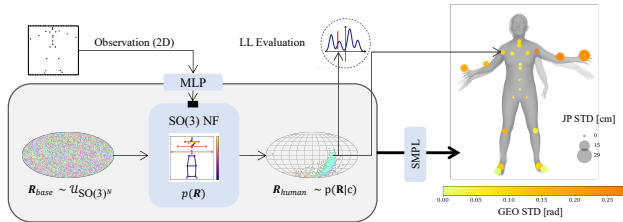


Figure 5. Overview of an example application of HuProSO3: Samples from $p(\mathbf{R}|\mathbf{c})$ are generated by propagating samples from a uniform distribution on the product space of $\text{SO}(3)$ through the normalizing flow. Partially given 2D key points serve as conditioning, where occluded joints are depicted in red. The prior $p(\mathbf{R})$ captures the statistical dependencies between different joints. The color of the blobs depict the standard deviation of the joint rotations computed for 20 samples. The blob size relates to the standard deviation of the joint position (JP) after applying forward kinematics.

compare the diversity of the predictions to the model extracted from [32] as proposed by [32] by computing the averaged Euclidean deviation from the sample mean for all generated samples. We evaluate for 10k random samples from the AMASS test datasets. Here, our model has a sample diversity of 11 mm and 109 mm for visible and occluded joints, respectively, while the ancestor-conditioned model by [32] results in a diversity of 39 mm and 98 mm for visible and occluded joints, respectively.

5-Point Evaluation. We also assess HuProSO3 on the 5-point evaluation benchmark [22, 35], where the model must infer all joint rotations based solely on the leaf joints. Despite not being explicitly trained for this specific condition, HuProSO3 successfully infers the pose distribution from the 3D keypoint positions of the leaf joints (see Tab. 4).

4.4. 2D to 3D Uplifting via $\text{SO}(3)$ Parameterization

In this experiment, we condition the learned density with 2D keypoint positions $\mathbf{x}_{2D} \in \mathbb{R}^{J \times 2}$ of the $J = 21$ SMPL joints and learn $p(\mathbf{R}|\mathbf{c})$, where $\mathbf{c} = g_{\text{feat}}(\mathbf{x}_{2D})$ is computed by an MLP. Then, the 3D pose is obtained by applying forward kinematics. We illustrate this setting in Fig. 5.

Metrics and Baselines. For the 2D to 3D uplifting application, we use MGEO and MPJPE as evaluation metrics, similar to the IK task. Our model is compared with Pose-NDF, GAN-S, and HF-AC. Unlike the previous experiments focusing on 3D keypoint positions (Eq. (10)), here we optimize for 2D keypoint positions.

Results. Evaluation results for the 2D to 3D uplifting task are detailed in Tab. 5, focusing on models using rotation representations for human pose. Unlike the IK task, inferring human poses from 2D data involves significant ambiguity. The results show that the considered optimization-based methods are performing worse since the optimization objective is less expressive and the results depend on the ini-

Table 5. MPJPE [mm] and MGEO [rad] results for the 2D to 3D uplifting task on the AMASS test dataset. For probabilistic models, results are shown for both a single sample and the average of 10 samples.

Method	MPJPE (1 10)	MGEO (1 10)
Pose-NDF [34]	133.1 -	0.522 -
GAN-S [4]	61.5 -	0.277 -
HF-AC [32]	74.4 / 56.0	0.346 / 0.278
Ours	32.8 23.4	0.209 0.153

tialization. Our model HuProSO3 outperforms other methods, affirming its effectiveness in probabilistically capturing ambiguous input conditions.

Fig. 5 qualitatively illustrates HuProSO3’s applications for partially given 2D key points. The generated samples depict the arising uncertainties accordingly. More samples are visualized in Fig. 13 in Appendix C.4.

5. Conclusion

We addressed the gap in normalized density models for high-dimensional product spaces of rotational manifolds, crucial in human pose modeling, which depends on rotational quantities. Our solution, HuProSO3, is a normalizing flow that effectively learns densities on product spaces of $\text{SO}(3)$ manifolds, capturing the rotational nature of human poses in a probabilistic way. Demonstrating its efficacy, HuProSO3 not only excels as an unconditional pose prior in generative applications but also adapts to applications that require conditioning on potentially incomplete information, as illustrated for the task of inverse kinematics and 2D to 3D uplifting via a rotational $\text{SO}(3)$ parameterization.

Limitations and Future Work. While effective in practice, the autoregressive structure in HuProSO3 has limitations in capturing all dependencies in a high-dimensional space, as it heavily depends on the permutation operation of the conditioning sequence. Moreover, sampling from a high-dimensional autoregressive model is slow as it scales linearly with the number of manifolds. Another limitation is that our model currently only supports products of $\text{SO}(3)$ manifolds. To better reflect the biomechanical structure of different joints, our approach could be extended to include other rotational manifolds. Additionally, the ability of our method to compute normalized densities opens up applications in human-robot collaboration. It also allows the integration as a prior or the injection of measurements in filtering and estimation problems, e.g., for human pose estimation based on key point measurements of the joints.

Acknowledgments. The authors would like to thank the Ministry of Science, Research and Arts of the Federal State of Baden-Württemberg for the financial support of the project within the InnovationCampus Future Mobility (ICM).

References

- [1] Ijaz Akhter and Michael J. Black. Pose-conditioned joint angle limits for 3D human pose reconstruction. In *Proceedings of the IEEE/CVF Conference on Computer Vision and Pattern Recognition (CVPR)*, 2015. 2
- [2] Ijaz Akhter and Michael J. Black. Keep it smpl: Automatic estimation of 3d human pose and shape from a single image. In *Proceedings of the European Conference on Computer Vision (ECCV)*, 2016. 2, 4
- [3] Hai Ci, Mingdong Wu, Wentao Zhu, Xiaoxuan Ma, Hao Dong, Fangwei Zhong, and Yizhou Wang. GFPose: Learning 3d human pose prior with gradient fields. *arXiv preprint arXiv:2212.08641*, 2022. 1, 5
- [4] Andrey Davydov, Anastasia Remizova, Victor Constantin, Sina Honari, Mathieu Salzmann, and Pascal Fua. Adversarial parametric pose prior. In *Proceedings of the IEEE/CVF Conference on Computer Vision and Pattern Recognition (CVPR)*, 2022. 2, 5, 6, 7, 8, 3
- [5] Laurent Dinh, David Krueger, and Yoshua Bengio. Nice: Non-linear independent components estimation. In *International Conference on Learning Representations (ICLR)*, 2015. 1
- [6] Laurent Dinh, Jascha Sohl-Dickstein, and Samy Bengio. Density estimation using real NVP. In *International Conference on Learning Representations (ICLR)*, 2017.
- [7] Conor Durkan, Artur Bekasov, Iain Murray, and George Papamakarios. Neural spline flows. In *Advances in neural information processing systems (NeurIPS)*, 2019. 1, 5
- [8] Luca Falorsi, Pim de Haan, Tim R. Davidson, and Patrick Forré. Reparameterizing distributions on lie groups. In *Proceedings of the twenty-second international conference on artificial intelligence and statistics*, 2019. 2, 6
- [9] Nicholas Fisher and A. Lee. Correlation Coefficients for Random Variables on a Unit Sphere or Hypersphere. *Biometrika*, 73, 1986. 1
- [10] Mathieu Germain, Karol Gregor, Iain Murray, and Hugo Larochelle. MADE: Masked autoencoder for distribution estimation. In *Proceedings of the 32nd international conference on machine learning (ICML)*, 2015. 4
- [11] Thorsten Glüsenskamp. Unifying supervised learning and VAEs – coverage, systematics and goodness-of-fit in normalizing-flow based neural network models for astroparticle reconstructions. *arXiv preprint arXiv:2008.05825*, 2023. 2
- [12] Durk P Kingma and Prafulla Dhariwal. Glow: Generative flow with invertible 1x1 convolutions. In *Advances in neural information processing systems (NeurIPS)*, 2018. 1
- [13] Ivan Kobyzev, Simon J.D. Prince, and Marcus A. Brubaker. Normalizing flows: An introduction and review of current methods. *IEEE Transactions on Pattern Analysis and Machine Intelligence*, 2021. 1
- [14] Nikos Kolotouros, Georgios Pavlakos, Dinesh Jayaraman, and Kostas Daniilidis. Probabilistic Modeling for Human Mesh Recovery. In *2021 IEEE/CVF International Conference on Computer Vision (ICCV)*, 2021. 1, 2
- [15] Hsi-Jian Lee and Zen Chen. Determination of 3D human body postures from a single view. *Computer Vision, Graphics, and Image Processing*, 1985. 1
- [16] Andreas M. Lehrmann, Peter V. Gehler, and Sebastian Nowozin. A Non-parametric Bayesian Network Prior of Human Pose. In *Proceedings of the IEEE/CVF International Conference on Computer Vision (ICCV)*, 2013. 2
- [17] Dong C. Liu and Jorge Nocedal. On the limited memory BFGS method for large scale optimization. *Mathematical Programming*, 1989. 6
- [18] Yulin Liu, Haoran Liu, Yingda Yin, Yang Wang, Baoquan Chen, and He Wang. Delving into Discrete Normalizing Flows on SO(3) Manifold for Probabilistic Rotation Modeling. In *Proceedings of the IEEE/CVF Conference on Computer Vision and Pattern Recognition (CVPR)*, 2023. 2, 3, 4
- [19] Naureen Mahmood, Nima Ghorbani, Nikolaus F. Troje, Gerard Pons-Moll, and Michael Black. AMASS: Archive of Motion Capture As Surface Shapes. In *Proceedings of the IEEE/CVF International Conference on Computer Vision (ICCV)*, 2019. 5, 1, 3
- [20] Kieran A. Murphy, Carlos Esteves, Varun Jampani, Srikumar Ramalingam, and Ameesh Makadia. Implicit-PDF: Non-Parametric Representation of Probability Distributions on the Rotation Manifold. In *Proceedings of the International Conference on Machine Learning (ICML)*, 2021. 3
- [21] Haruki Nishimura, Boris Ivanovic, Adrien Gaidon, Marco Pavone, and Mac Schwager. Risk-sensitive sequential action control with multi-modal human trajectory forecasting for safe crowd-robot interaction. *CoRR*, abs/2009.05702, 2020. 1
- [22] Boris N. Oreshkin, Florent Bocquet, Félix G. Harvey, Bay Raitt, and Dominic Laflamme. ProtoRes: Proto-residual network for pose authoring via learned inverse kinematics. In *International Conference on Learning Representations (ICLR)*, 2022. 2, 8
- [23] George Papamakarios, Theo Pavlakou, and Iain Murray. Masked autoregressive flow for density estimation. In *Advances in neural information processing systems (NeurIPS)*, 2017. 2, 4, 5
- [24] George Papamakarios, Eric T. Nalisnick, Danilo Jimenez Rezende, Shakir Mohamed, and Balaji Lakshminarayanan. Normalizing Flows for Probabilistic Modeling and Inference. *Journal of Machine Learning Research*, 2019. 1, 4
- [25] Georgios Pavlakos, Vasileios Choutas, Nima Ghorbani, Timo Bolkart, Ahmed A. Osman, Dimitrios Tzionas, and Michael J. Black. Expressive Body Capture: 3D Hands, Face, and Body From a Single Image. In *Proceedings of the IEEE/CVF Conference on Computer Vision and Pattern Recognition (CVPR)*, 2019. 2, 6, 7, 5
- [26] Davis Rempe, Tolga Birdal, Aaron Hertzmann, Jimei Yang, Srinath Sridhar, and Leonidas J. Guibas. HuMoR: 3D Human Motion Model for Robust Pose Estimation. In *Proceedings of the IEEE/CVF International Conference on Computer Vision (ICCV)*, 2021. 6, 7, 5
- [27] Danilo Jimenez Rezende, George Papamakarios, Sebastien Racaniere, Michael Albergo, Gurtej Kanwar, Phiala Shanahan, and Kyle Cranmer. Normalizing flows on tori and

- spheres. In *Proceedings of the International Conference on Machine Learning (ICML)*, 2020. 2
- [28] Yossi Rubner, Carlo Tomasi, and Leonidas J. Guibas. The Earth Mover’s Distance as a Metric for Image Retrieval. *International Journal of Computer Vision*, 2000. 1
- [29] Tim Salzmann, Marco Pavone, and Markus Ryll. Motron: Multimodal Probabilistic Human Motion Forecasting. In *Proceedings of the IEEE/CVF Conference on Computer Vision and Pattern Recognition (CVPR)*, 2022. 1
- [30] Akash Sengupta, Ignas Budvytis, and Roberto Cipolla. Hierarchical kinematic probability distributions for 3D human shape and pose estimation from images in the wild. In *Proceedings of the IEEE/CVF International Conference on Computer Vision (ICCV)*, 2021. 2
- [31] Akash Sengupta, Ignas Budvytis, and Roberto Cipolla. Probabilistic 3D Human Shape and Pose Estimation from Multiple Unconstrained Images in the Wild. In *Proceedings of the IEEE/CVF Conference on Computer Vision and Pattern Recognition (CVPR)*, 2021.
- [32] Akash Sengupta, Ignas Budvytis, and Roberto Cipolla. HuManiFlow: Ancestor-Conditioned Normalising Flows on SO(3) Manifolds for Human Pose and Shape Distribution Estimation. In *Proceedings of the IEEE/CVF Conference on Computer Vision and Pattern Recognition (CVPR)*, 2023. 1, 2, 6, 7, 8, 4, 5
- [33] Vincent Stimper, David Liu, Andrew Campbell, Vincent Berenz, Lukas Ryll, Bernhard Schölkopf, and José Miguel Hernández-Lobato. normflows: A PyTorch Package for Normalizing Flows. *Journal of Open Source Software*, 2023. 2, 5
- [34] Garvita Tiwari, Dimitrije Antić, Jan Eric Lenssen, Nikolaos Sarafianos, Tony Tung, and Gerard Pons-Moll. PoseNDF: Modeling Human Pose Manifolds with Neural Distance Fields. In *Proceedings of the European Conference on Computer Vision (ECCV)*, 2022. 2, 5, 6, 7, 8
- [35] Vikram Voleti, Boris N. Oreshkin, Florent Bocquetlet, Félix G. Harvey, Louis-Simon Ménard, and Christopher Pal. SMPL-IK: Learned Morphology-Aware Inverse Kinematics for AI Driven Artistic Workflows. *arXiv preprint arXiv:2208.08274*, 2022. 2, 8
- [36] Hongyi Xu, Eduard Gabriel Bazavan, Andrei Zanfir, William T. Freeman, Rahul Sukthankar, and Cristian Sminchisescu. GHUM & GHUML: Generative 3D Human Shape and Articulated Pose Models. In *Proceedings of the IEEE/CVF Conference on Computer Vision and Pattern Recognition (CVPR)*, 2020. 1, 2, 5
- [37] Andrei Zanfir, Eduard Gabriel Bazavan, Hongyi Xu, William T. Freeman, Rahul Sukthankar, and Cristian Sminchisescu. Weakly Supervised 3D Human Pose and Shape Reconstruction with Normalizing Flows. In *Proceedings of the European Conference on Computer Vision (ECCV)*, 2020. 5
- [38] Yi Zhou, Connelly Barnes, Jingwan Lu, Jimei Yang, and Hao Li. On the Continuity of Rotation Representations in Neural Networks. In *Proceedings of the IEEE/CVF Conference on Computer Vision and Pattern Recognition (CVPR)*, 2019. 2, 3, 4

Normalizing Flows on the Product Space of SO(3) Manifolds for Probabilistic Human Pose Modeling

Supplementary Material

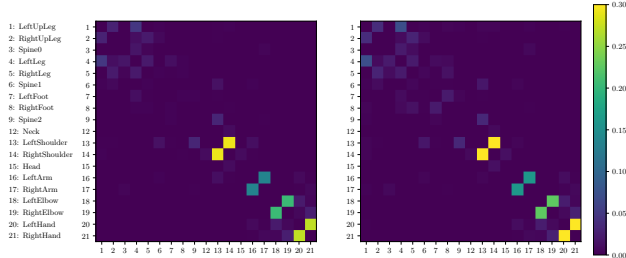


Figure 6. Spherical correlation coefficient of samples from HuProSO3 (left) and from AMASS training dataset (right), excluding toe bases and root joints. Entries on the diagonal are set to zero because their correlation coefficient $\hat{\rho}_{XY} = 1$ is always equal to one. The coefficients are computed using 100k samples.

To complement the main paper, this supplementary material delves into additional aspects not covered in detail previously. We include an analysis of the AMASS database, provide extended qualitative and quantitative evaluations, and share details on the implementation and training.

A. Dataset Analysis

Given that both the development and assessment of our method are grounded in a statistical analysis of the AMASS database, we present the key findings and insights from this analysis in this section.

A.1. Correlation Between Different Joints

Computing a correlation or dependence coefficient on SO(3) is not straightforward. Hence, we use a unit quaternion representation of orientations and follow [9] to compute a spherical correlation coefficient

$$\hat{\rho}_{XY} = \frac{\det\left(\frac{\sum_i X_i Y_i^T}{n}\right)}{\sqrt{\det\left(\frac{\sum_i X_i X_i^T}{n}\right) \det\left(\frac{\sum_i Y_i Y_i^T}{n}\right)}} \quad (12)$$

for the n samples X_i, Y_i on the 3-sphere \mathcal{S}^3 , on which all quaternions reside. We visualize the spherical correlation coefficients for all dynamic joints of the AMASS database (excluding toe bases and the root orientation) in Fig. 6. The illustration depicted in Fig. 7 provides a better intuition of these correlation coefficients, comparing the correlation coefficients along the kinematic tree and for all joints. Notably, high correlations are observed particularly for joints at different leaves of the kinematic tree, such as for the left

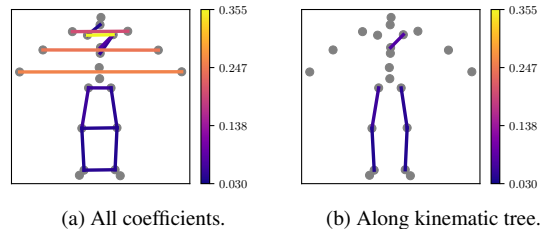


Figure 7. Color-coded spherical correlation coefficients illustrated along a skeleton model of the human body. For clarity, only the coefficients with a value $\hat{\rho}_{XY} > 0.03$ are depicted.

and right arm joints. We note that the used correlation coefficient only captures certain dependencies on the 3-sphere.

A.2. Distribution Gaps for the AMASS Datasets

Evaluating an unconditional prior typically assumes *iid* samples in training and test datasets, which is not the case for the AMASS [19] database. To compare the distributions of two datasets based on a sample-based similarity metric of the rotations, we compute the earth mover’s distance (EMD) [28] using the geodesic distance as the distance measure. We compare the EMDs for individual joints and for all joints for the common AMASS datasets split [19] in Fig. 8 and the EMD between various datasets of the AMASS database in Fig. 9. For computational reasons, we use only 2k samples for the transport problem, acknowledging potential inaccuracies in higher dimensions. Nevertheless, the distribution gap is highlighted because the entries of the correlation matrix that correspond to the auto-correlation are markedly lower than the cross-correlation. This aligns with the notable performance disparity between training and test datasets shown in the main paper (Tab. 1).

B. Implementation and Training Details

In the following, we elucidate the implementation and training details for HuProSO3 and the integration of the other evaluated methods.

B.1. HuProSO3

We trained the following HuProSO3 models: one as an unconditional prior, one for inverse kinematics, one for inverse kinematics with randomly occluded 3D key points, and one for 2D to 3D uplifting.

Architecture. The normalizing flow architecture for learning the density $p(\mathbf{R})$ is consistent across all experi-

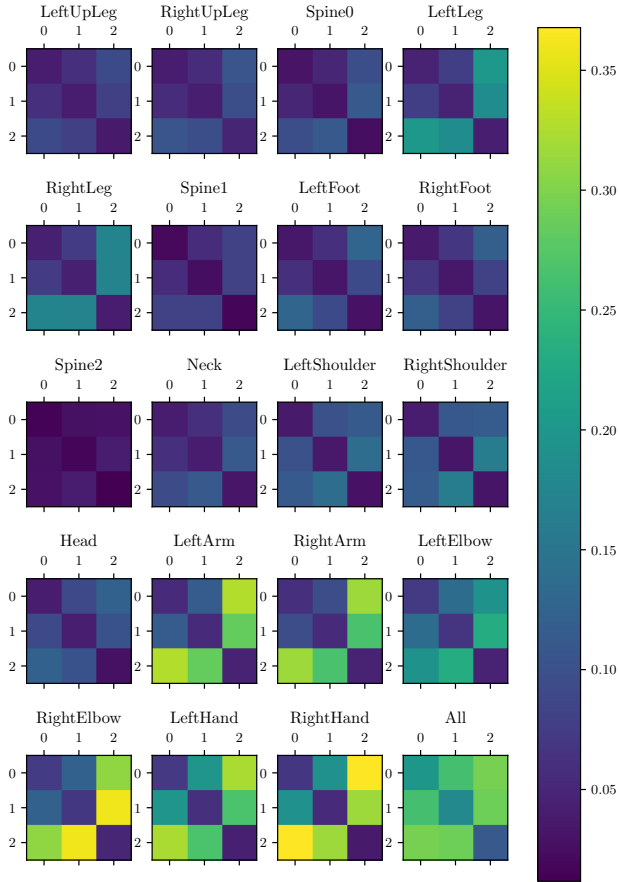


Figure 8. Earth mover’s distance between AMASS training (0), validation (1), and test (2) datasets based on the geodesic distance for all dynamic SMPL joints and when comparing *All* joints. For the *All* category, the EMD is computed using the average geodesic distance across multiple joint rotations.

ments. We use 12 Möbius coupling layers, with each layer (except the final one) followed by a quaternion affine transformation, totaling 11 quaternion affine layers. The parameters of the Möbius transformation are computed by an MLP $g_{c-M}(\cdot)$ with three hidden layers and ReLU activations and a hidden dimension of 16. For the presented applications that require conditioning (inverse kinematics and 2D to 3D uplifting), an MLP $c = g(c_{\text{feat}})$ computes the relevant features from the input context vector c_{feat} . We use an MLP with one hidden layer and a hidden dimension of 64. The output dimension of the feature is $c \in \mathbb{R}^{64}$. The complete model that is conditioned on the 3D pose has around 1.5 million parameters.

Training. Our models are trained with a batch size of 1k, utilizing the Adam optimizer. We set the initial learning rate to $5e-3$ and employ a step learning rate scheduler with a multiplicative factor of 0.5 for learning rate decay.

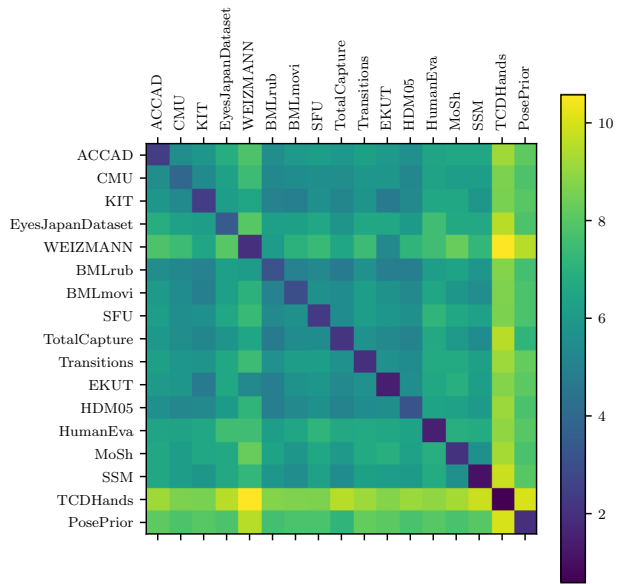


Figure 9. Earth mover distances between various datasets in the AMASS database, computed based on the sum of the geodesic distances of all dynamic joints of the AMASS database.

Run time. Sampling from an autoregressive model is slow and scales with the number of dimensions. Parallelizing the evaluation of the model is in general possible. However, our current implementation does not support this. Therefore, evaluating one batch requires around 1.1s on a NVIDIA A40 GPU, while sampling one batch takes around 2.1s.

B.2. Learning and Optimizing Baseline Methods

We compare our method with implementations of VPoser [25], GAN-S [4], Pose-NDF [34], and HuManiFlow [32]. We use the pre-trained models for the priors VPoser, GAN-S, and Pose-NDF. The normalizing flow based on the 6D representation is implemented using the *CircularAutoregressiveRationalQuadraticSpline* module of the normflows library [33], with the PDF defined on $x \in \mathbb{R}^{6-19}$.

For conditional tasks, we optimize GAN-S and Pose-NDF for inverse kinematics and 2D to 3D uplifting as outlined in the main paper in Sec. 4.2 based on 21 SMPL joints. For GAN-S, we utilize the L-BFGS optimizer, set the learning rate to 1 and perform 500 iterations. We use the existing Pose-NDF repository to optimize for occluded joints, and we mask the joint positions in case of occlusions as outlined in Eq. (11) in the main paper.

We train the extracted model of HuManiFlow [32] using the Adam optimizer with a learning rate of $5e-5$ with a step learning rate scheduler and step factor of 0.5, and a batch size of 500 until convergence. We apply the same masking strategy as for HuProSO3.

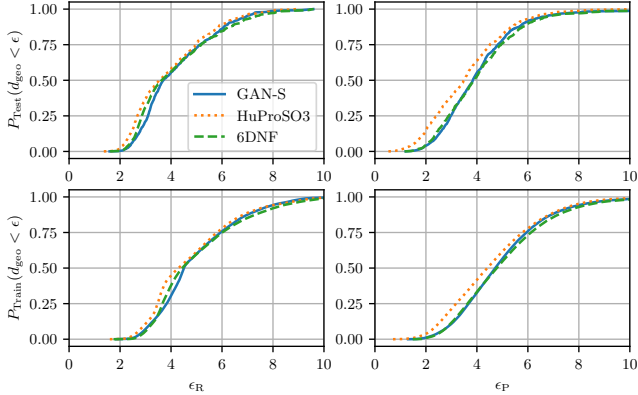


Figure 10. Precision (P) and recall (R) curves for AMASS training and test dataset based on the summed geodesic distances as presented in the main paper, computed for GAN-S, HuProSO3, and 6D normalizing flow. Higher values indicate better quality in all charts.

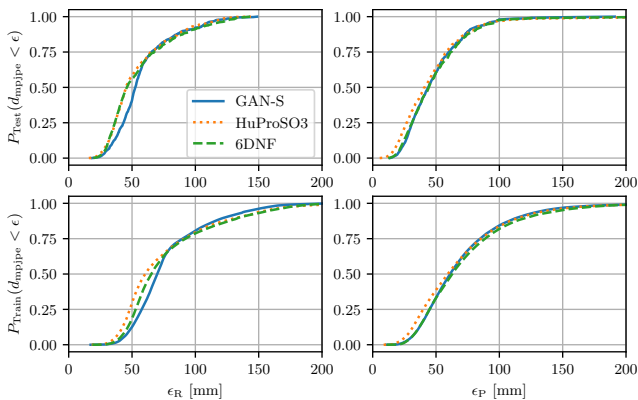


Figure 11. Precision (P) and recall (R) curves for the AMASS training and test datasets based on the MPJPE metric, computed for GAN-S, HuProSO3, and 6D normalizing flow. Higher values indicate better quality in all charts.

B.3. Visualization Techniques

In Fig. 5, we adopt the visualization technique introduced by [20] to display samples on $SO(3)$. A sample on $SO(3)$ is visualized by projecting it onto a 2-sphere and visualizing the third rotation angle through color coding.

C. Additional Qualitative Results

C.1. Correlation Coefficients for Learned Prior

To demonstrate that our prior has effectively learned correlations between different joint rotations, we plot the spherical correlation coefficients computed on sampled poses from the prior in figure Fig. 6 next to spherical correlation coefficients computed from samples of the datasets.

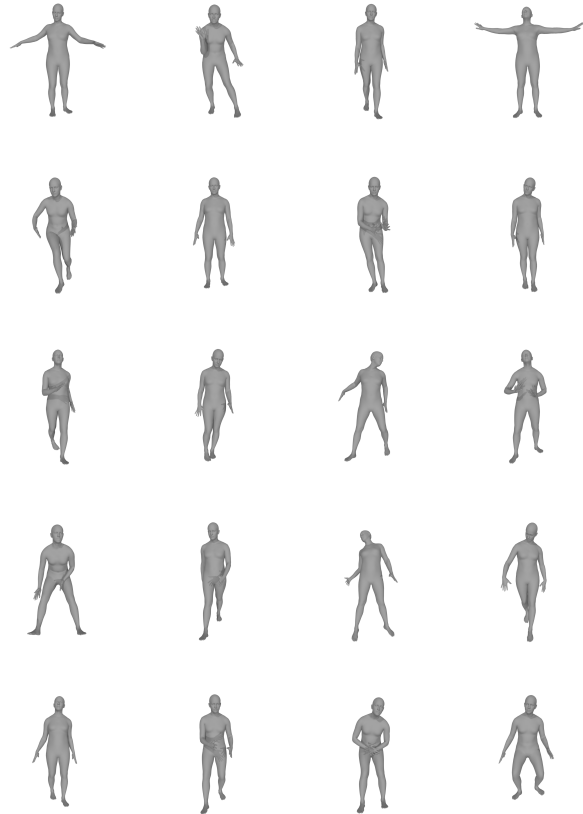


Figure 12. Renderings of randomly sampled human poses from the unconditional HuProSO3 prior.

Table 6. Summary of precision and recall statistics for the AMASS database [19], both on test and training datasets. The values indicate the MPJPEs [mm] for all SMPL joints between samples from the dataset and the evaluated pose prior after applying forward kinematics.

	Test (mean [median])		Train (mean [median])	
	Recall	Precision	Recall	Precision
GAN-S [4]	50.6 [48.4]	68.7 [64.2]	39.7 [35.0]	56.2 [49.7]
6D NF	46.3 [39.9]	65.8 [57.8]	39.4 [34.2]	57.2 [49.4]
Ours	45.4 [40.2]	61.2 [52.1]	34.3 [28.8]	51.3 [43.2]

C.2. Precision Recall Curves

To evaluate the priors, we compute the precision and recall curves. We plot the curves in Fig. 10. To assess the priors, we compute and plot the precision and recall curves, as shown in Fig. 10 and Fig. 11. This comparison, similar to the one presented in Tab. 1 of the main paper, is based on the MPJPE metric. Additionally, the mean and median values of these metrics are detailed in Tab. 6.

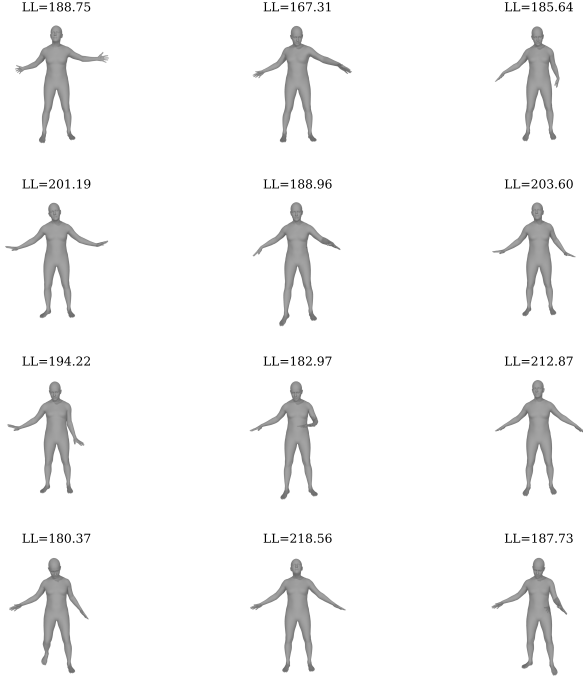


Figure 13. Renderings of human poses sampled from the predicted distribution, conditioned on the 2D key point positions of all joints, excluding the left arm and the right leg. The log likelihood corresponding to a normalized density is displayed above the considered sample.

C.3. Rendered Samples from Unconditional Prior

To demonstrate HuProSO3’s capability as a generative model for sampling realistic and diverse human poses, we present renderings of randomly selected samples in Fig. 12.

C.4. Rendered Samples from 2D to 3D Uplifting

Based on the setting and conditioning in Fig. 5, we render 12 poses that are sampled from the learned distribution $p(\mathbf{R}|\mathbf{c})$ in Fig. 13, where \mathbf{c} is derived from 2D key points with the left arm and the right leg occluded. These samples, displayed in Fig. 13, reveal that while the model often predicts straight right legs, the left arm’s pose varies significantly, which follows the training dataset’s distribution. For joints where the given 2D key point positions allow inferring their rotations, the estimates show less variability, as we also visualize in Fig. 5 of the main paper for the standard deviation of the joint’s positions and rotations.

Optimization-based methods are limited to inferring a single pose from occluded key points. While this approach might yield accurate results on average, as reflected in mean metrics, it fails to capture the inherent ambiguity in these scenarios.

Table 7. Log likelihood evaluation for inverse kinematics (IK), rotation distribution estimation given 2D key points (2D to SO(3)), and an unconditional prior. Unless specified otherwise, results pertain to the AMASS test dataset.

Method	IK	2D to SO(3)	Prior	Prior (Train)
HuManiFlow [32]	100.8	83.6	-	-
Ours	217.5	202.2	137.6	184.7

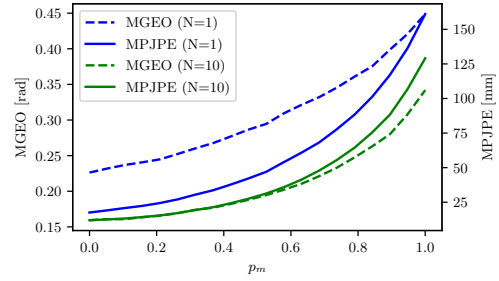
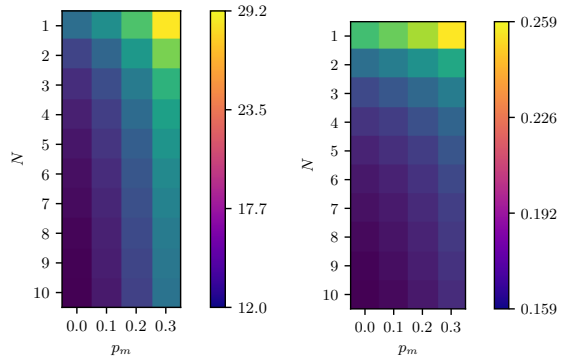


Figure 14. MGE0 and MPJPE for a variation of the mask probability p_m based on one sample and the mean over 10 samples drawn from HuProSO3 conditioned on partially given 3D key point information.



(a) Positional error MPJPE [mm]. (b) Rotational error MGE0 [rad].

Figure 15. MPJPEs and MGE0s for different masking probabilities p_m and numbers of samples from the learned distribution N . The metrics are calculated based on the mean of the sampled poses by computing the average rotation for each joint.

D. Additional Quantitative Results

D.1. Evaluation of Likelihood

We evaluate the likelihoods for the unconditional prior with HuProSO3 and for conditional distributions for HuProSO3 and the HuManiFlow approach in Tab. 7. For the unconditional prior, the likelihood evaluations also reveal a significant gap between the training and test distributions.

D.2. Comparison to Pose-NDF as Pose Prior

We evaluate Pose-NDF as a pose prior by computing the precision and recall statistics. In a first experiment, we evaluate when initializing with noise. However, this does not

Table 8. Summary of precision and recall statistics for the AMASS database [19], both on test and training datasets. The reported values represent the cumulative geodesic distances for all joint rotations between samples from the dataset and the evaluated pose prior. Pose-NDF 1 was optimized using random initialization, Pose-NDF 2 using slightly noised poses from the AMASS test dataset.

	Test (mean [median])		Train (mean [median])	
	Recall	Precision	Recall	Precision
P-NDF 1	17.7 [17.7]	14.5 [14.4]	17.5 [17.2]	14.7 [14.4]
P-NDF 2	4.83 [4.77]	5.63 [5.42]	6.11 [5.92]	6.88 [6.65]
Ours	3.44 [2.95]	4.24 [3.71]	2.93 [2.64]	3.90 [3.59]

Table 9. Summary of precision and recall statistics for the AMASS database [19], both on test and training datasets. The reported values represent the cumulative geodesic distances for all joint rotations between samples from the dataset and the evaluated pose prior.

	Test (mean [median])		Train (mean [median])	
	Recall	Precision	Recall	Precision
GAN-S [4]	3.76 [3.34]	4.51 [4.23]	3.57 [3.34]	4.38 [4.13]
6D NF	3.66 [3.16]	4.50 [4.00]	3.55 [3.32]	4.42 [4.10]
Ours	3.44 [2.95]	4.24 [3.71]	2.93 [2.64]	3.90 [3.59]

Table 10. Comparison to GFPose-rot: Minimum MGEO and minimum MPJPE are computed based on 20 generated samples for the occlusion of leg (L), arm and hand (A), and upper arm (S). The results are presented for 10k random samples from the AMASS test datasets. The GEO metrics are averaged over 21 joints.

Method	minMGEO			minMPJPE		
	L	A	S	L	A	S
GFPose-rot (N=1)	0.104	0.108	0.089	7.9	14.3	4.9
GFPose-rot (N=20)	0.103	0.107	0.088	7.8	14.1	4.8
Ours (N=1)	0.217	0.254	0.208	20.8	39.0	18.7
Ours (N=20)	0.070	0.081	0.067	5.7	11.2	5.2

result in realistic poses since Pose-NDF generates realistic poses when the initialized poses are close to the training distribution. In a second experiment, we add a small amount of noise to poses of the test distribution ($\sigma_{\text{noise}} = 0.1$), which provides realistic poses. However, such an initialization inherently biases the optimization towards in-distribution samples. Therefore, it is highly depending on the similarity between training and test distribution.

D.3. Comparison to GFPose-rot

Directly comparing to GFPose [3] is not possible since it was not trained on the AMASS database and it is parameterized with joint positions. Therefore, we adapt the implementation of GFPose and we train it on the AMASS database using the axis-angle representation using the same hyperparameters as in the original repository. For the occlusions, we apply the same masking strategy as in our imple-

Table 11. Comparison of per-vertex errors [mm] across various occluded joints in the AMASS test dataset: left leg (L), left arm and hand (A+H), and right shoulder and upper arm (S+UA). The results are based on 60 frames as reported in [34].

Method	L	A+H	S + UA
VPoser [25]	25.3	85.1	99.8
HuMoR [26]	56.0	78.3	47.5
Pose-NDF [34]	24.9	78.1	76.3
Ours (N=10)	34.0	57.5	34.5

mentations. We follow [3] and evaluate using the minimum error sample. We use 10 times fewer samples than GFPose (N=20) and we report the results for minimum geodesic distance and joint position error in Tab. 10. In our experiments, GFPose-rot collapses to the mean pose. While our results are worse for single sample evaluations, our model provides more diverse samples than GFPose-rot.

Here, a disadvantage of our model becomes apparent: Since our base distribution is uniform on $SO(3)$, computing the mode as when considering a Gaussian distribution is not possible. This might be a reason, why generating an individual sample does not achieve competing results.

While GFPose-rot achieves partially better results, it does not provide a normalized density.

D.4. Per-Vertex Errors for Inverse Kinematics and Occluded Joints

We compare HuProSO3’s per-vertex error performance with HuMoR [26] using *TestOpt*, VPoser [25], and Pose-NDF [34] for 60 frames, following the protocol in [34]. We present the per-vertex error results for inverse kinematics and occluded joints in Tab. 11. While the optimization-based methods achieve a better performance for the MPJPE metric, the presented results in Tab. 11 also support that the wrong rotation estimates result in worse performance when comparing all mesh vertices on the rendered human.

D.5. Evaluations for Varying Numbers of Samples

We present additional evaluation results for varying numbers of samples that are used for computing positional and rotational errors in Fig. 15 and Fig. 14. Fig. 15 extends the visualizations from Fig. 14 by presenting MPJPE and MGEO metrics for different masking probabilities and sample counts drawn from HuProSO3, with each joint masked with a probability of p_m .

Baselines and Setup. In addition to HuProSO3, as detailed in the main paper, and the model based on the HuManiFlow implementation, we also compare with an implementation that uses normalizing flows defined on $SO(3)$ as for HuProSO3, but with fixed ancestor-conditioning as suggested in [32]. We train this model following the same strategy as for HuProSO3. For evaluation, joints are ran-

domly masked with a probability of $p_m = 0.3$. We present the errors for the average joint rotations (as in the main paper) and, additionally, based on the pose out of the N sampled poses that results in the lowest considered error metric (minimum error sample). We compute all results based on 10k randomly drawn samples from the AMASS test dataset.

Discussion. Our analysis reveals that normalizing flows designed with the $SO(3)$ modeling approach seem to more effectively capture the joint distribution than the approach by [8] applied in [32]. While the error for a single sample ($N = 1$) is similar across both ancestor-conditioned models (*SO3 AC* and *HF AC*) for the selected masking strategy, the $SO(3)$ -based model yields lower minimum errors with an increased number of samples. However, ancestor-conditioning along the kinematic tree does not fully capture all statistical dependencies. Consequently, HuProSO3, which is not limited to fixed conditioning sequences and operates on the product space of all $SO(3)$ manifolds, demonstrates notably lower minimum and average pose errors, reflecting its superior capability in learning dependencies of the joint rotations.